J Mater Sci (2010) 45:2553–2557
DOI 10.1007/s10853-010-4225-x

Thermal effect of bainite/martensite duplex-phase steel under ultrasonic fatigue testing

Y. B. Liu · S. X. Li · Z. G. Yang · Y. D. Li · Y. Yu · J. L. Gu · B. Z. Bai · G. X. Cai

Received: 27 August 2009 / Accepted: 11 January 2010 / Published online: 26 January 2010

Abstract Ultrasonic fatigue testing was conducted for two bainite/martensite duplex-phase high strength steels with the same chemical compositions and different heat treatments. In this study, a very interesting result was that the obvious thermal effect could be found in some specimens of one steel. Their specimens' surfaces were oxidized because of high temperature during the fatigue tests, and the surface of gage section was changed into snuff color. On the other hand, none of the other specimens was oxidized. The fracture surfaces of oxidized specimens became rough. The results showed that the obvious thermal effect was related to the fatigue crack propagation after fish-eye formation.

Introduction

Ultrasonic fatigue testing [1–3] is a powerful tool for conducting very high cycle fatigue tests because of its extremely high frequency of 20 kHz. Large numbers of materials have been conducted under ultrasonic fatigue testing for time saving [4–11]. For those tests, frequency and thermal effects have to be considered. Results in the literature [11–14] indicate that the frequency effect is small in most cases for high strength steels at low stress amplitude. There are two common methods to solve the problem of temperature rising: a compressed air cooling and intermittent loading. When one or both of the methods are adopted, the testing temperature is limited at a reasonable range, for instance, 50–70 °C [12].The results show good agreement with conventional fatigue tests [11–13].

In all described investigations above, the steel specimens are tested in quenched and tempered condition. On the other hand, few bainite/martensite duplex-phase high strength steels have been conducted under ultrasonic fatigue testing. Because of containing soft bainite, their thermal effect might be different from that of the quenched and tempered high strength steels whose microstructure is mainly tempered martensite. The main objective of this article is to investigate thermal effect of bainite/martensite duplex-phase high strength steels under ultrasonic fatigue testing.

Y. B. Liu (✉) · S. X. Li · Z. G. Yang · Y. D. Li
Shenyang National Laboratory for Materials Science, Institute of Metal Research, Chinese Academy of Sciences, 110016 Shenyang, People's Republic of China
e-mail: ybliu@imr.ac.cn

Y. Yu · J. L. Gu · B. Z. Bai
Laboratory of Advanced Materials, Department of Materials Science and Engineering, Tsinghua University, 100084 Beijing, People's Republic of China

G. X. Cai
Department of Analyses and Testing, Institute of Metal Research, Chinese Academy of Sciences, 110016 Shenyang, People's Republic of China

Materials and experiments

Ingots of bainite/martensite duplex-phase high strength steels with the same chemical compositions and different processing routes were rolled and forged into round bars of 16 mm in diameter and named as R and F, respectively. F was isothermal annealed twice at 600 °C and R was without isothermal annealing. The chemical composition was 0.23C–1.9Si–2.3Mn–0.6Cr–0.038Nb expressed as mass%. Details of the heat treatment for the two steels are: austenitizing at 900 °C for 20 min, followed by directly air cooling and then tempering in 280 °C for 120 min. The

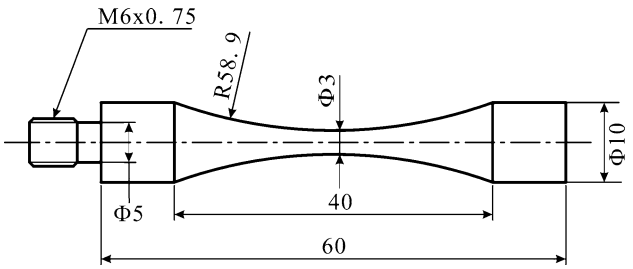

Fig. 1 Dimensions of fatigue test specimen

microstructure of both steels was a multi-phase of bainite (about 20%), martensite, and retained austenite (about 4.5%). Since the martensite and bainite are the two major phases, it is named as duplex-phase steel. For R and F specimens, the 0.2 Pct proof stress, ultimate tensile strength and elongation were 1318, 1627 MPa and 13%, and 1300, 1530 MPa and 11%, respectively.

The dimension of fatigue test specimen used in the present investigation is shown in Fig. 1. Fatigue tests were conducted on a Shimadzu USF-2000 at a resonance frequency of 20 kHz and a stress ratio of $R = -1$ at room temperature in air. The specimens were cooled by a compressed air circulation at 20 °C. The loading pattern used in this study was consisted of a 150 ms duty period and a 600-ms pause period. The specimens were conducted until 5×10^8 cycles on account of time except two F specimens until 1×10^9 cycles. The S–N data for both steels are shown in Fig. 2. All fracture surfaces of failed specimens were examined in an SEM. In order to measure the temperature on the specimen surface, an infrared camera is used, which is made up of a matrix of 752 × 480 pixels. The spectral range of wavelengths is between 8 and 14 μm. The spatial resolution is 0.60 mm per pixel and the acquisition frequency is 5 Hz.

Results and discussion

In this study, a very interesting result was that the obvious thermal effect can be found in some specimens of F steel.

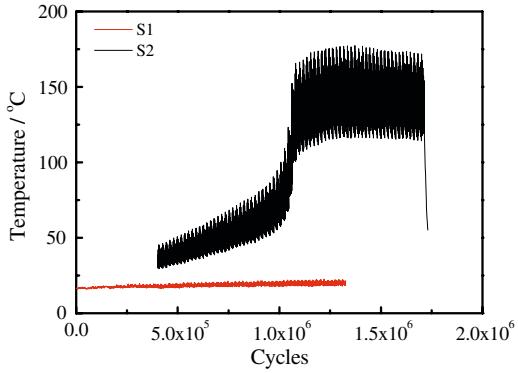

Fig. 3 Temperature evolution on the specimens surfaces during ultrasonic fatigue tests. S1 was tested under 650 MPa and the temperature measurement was stopped after 1.3×10^6 fatigue cycles. S2 was tested under 700 MPa

Normally, for quenched and tempered martensite steels, the thermal effect usually could be neglected in the testing conditions of compressed air cooling and a 150-ms pause period with a 150-ms duty period [4–8]. However, for some specimens of F, the thermal effect was so severe that their surfaces were oxidized because of higher temperature resulted during the fatigue tests, indicated in a dashed rectangular shown in Fig. 2b. As shown in Fig. 3, the temperature evolution of two F specimens was measured with the infrared camera during ultrasonic fatigue test. S1 shown in Fig. 2b which was not broken was tested under 650 MPa. Since the temperature remained stationary because of a balance between the heat source and the energy lost by conduction and convection, the temperature measurement was stopped after 1.3×10^6 fatigue cycles and the fatigue test was kept until 5×10^8 cycles. S2 shown in Fig. 2b was tested under 700 MPa. The temperature curve of the second specimen consisted of three zones (see Fig. 3): initially, a gradual rise in temperature occurred up to 10^6 fatigue cycles and the temperature was approached to 90 °C. This zone was actually similar to the experimental results reported by Wang and Bathias [14]; then an abrupt increase in temperature from 90 up to 160 °C was followed in the next 5×10^4 fatigue cycles; after that, the curve

Fig. 2 The S–N data for R (**a**) and F (**b**) steels

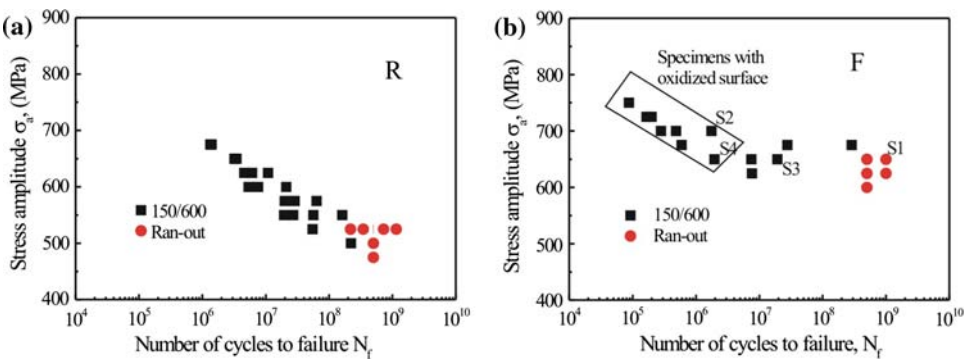

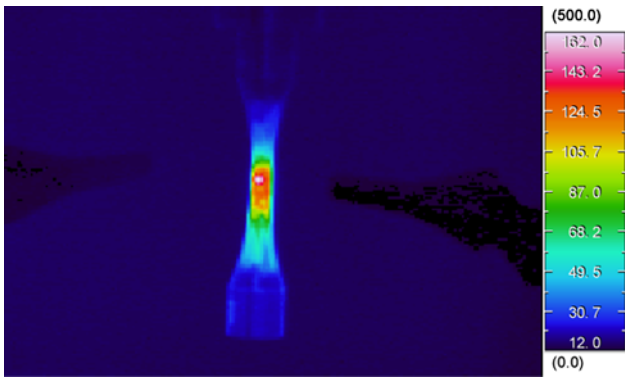

Fig. 4 Temperature field on the specimen surface just before fracture ($\sigma_a = 700$ MPa, $N_f = 1.73 \times 10^6$)

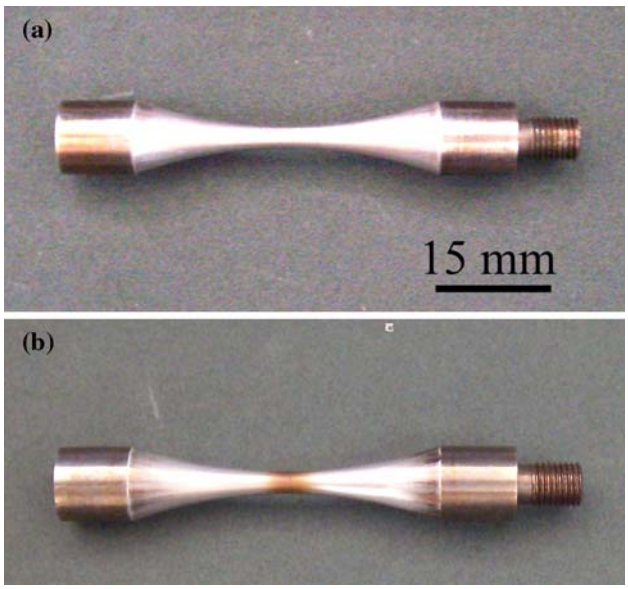

Fig. 5 The specimen surface for F steel. **a** No oxidized specimen S3 ($\sigma_a = 650$ MPa, $N_f = 1.93 \times 10^7$) and **b** oxidized specimen S4 ($\sigma_a = 650$ MPa, $N_f = 1.95 \times 10^6$)

became almost horizontal which had not been reported by other researchers. The maximum temperature was 180 °C for the entire period. It should be noticed that the actual maximum temperature in some local area, for instance crack tip, would be higher than 180 °C because that is the average temperature in a space of 0.60 mm and it takes 0.2 s to acquire the value while the compressed air is cooling down the specimen. The fluctuation of the temperature is caused by intermittent loading and compressed air cooling. The thermographs of Fig. 4 showed the temperature field on the specimen surface just before fracture. In order to investigate the relationship between oxidized surface and the fatigue process, another two of F specimens under the same stress amplitude of 650 MPa, no oxidized S3 and oxidized S4 shown in Fig. 2b, were taken as examples. The oxidized surface for S4 was shown in Fig. 5b. The surface of gage section was changed into snuff color (Fig. 5b) while that of S3 remained silvery (Fig. 5a). Figure 6 shows the fracture surface morphologies for S3 and S4 with some similar features and some substantially different characteristics. Both fatigue cracks initiated at subsurface and formed fish-eyes with similar sizes and similar fracture surface morphologies within fish-eye as indicated by the arrows in Figs. 6a, b. However, after fish-eye formation, the crack propagations were quite different. As shown in Fig. 6a for S3, beyond the fish-eye, the fracture surface remained flat, which means the crack propagation kept slow and stable. On the other hand, beyond the fish-eye for S4, the fracture surface became rough, which means that the crack propagated rapidly and unstably as shown in Fig. 6b. The two specimens underwent the similar process from crack initiation to forming fish-eye; the major difference between S3 and S4 was whether they possessed stable crack propagation stages. The fatigue life of S3 was about ten times longer than that of S4 as shown in Fig. 2b. It should be noticed that the difference, with or without a stable crack propagation, was not fully responsible for the difference of fatigue life. It was noted that the fatigue life strongly related to the inclusion size for high strength steels [15]. Because the inclusion size was substantially reduced by electroslag remelting, the crack initiated from large bainite. Therefore, if we consider that the bainite plays a similar role as inclusion, the difference of bainite size at initiation site will definitely lead to the major part of difference of fatigue life. As shown in Fig. 6c, we discriminated that the crack initiated from the brightest area as indicated by the triangle for S3 (about 14 μm in equivalence diameter). The initiation site for S4 was indicated by the circle (about 32 μm in diameter) in Fig. 6d. Comparison of S4 with S3, the larger bainite as crack initiation site, the shorter fatigue life was.

There are several types of heat sources: the thermo-elasticity [16], the hysteretic effects, and the plastic dissipation of the mechanical energy into heat [17–19]. The temperature change (ΔT_{el}) that occurs during elastic loading varies in proportion to the applied stress ($\Delta\sigma$) due to the Joule–Thomson effect [16].

$$\Delta T_{el} = -(\alpha/\rho c) T_0 \Delta\sigma \quad (1)$$

where α is thermal expansion coefficient, ρ is density, c is specific heat, and T_0 is initial temperature. ΔT_{el} is in general very low (less than 1 °C in our case). As the stress amplitude approaches the yield strength, the area within the stress–strain hysteresis loop increases duo to additional micro-plastic or plastic deformations and the mechanical work described by the hysteresis loop is primarily converted into heat. Due to the stress amplitudes of this test is much less than the yield strength, the temperature rise caused by hysteretic effect is supposed to be small.

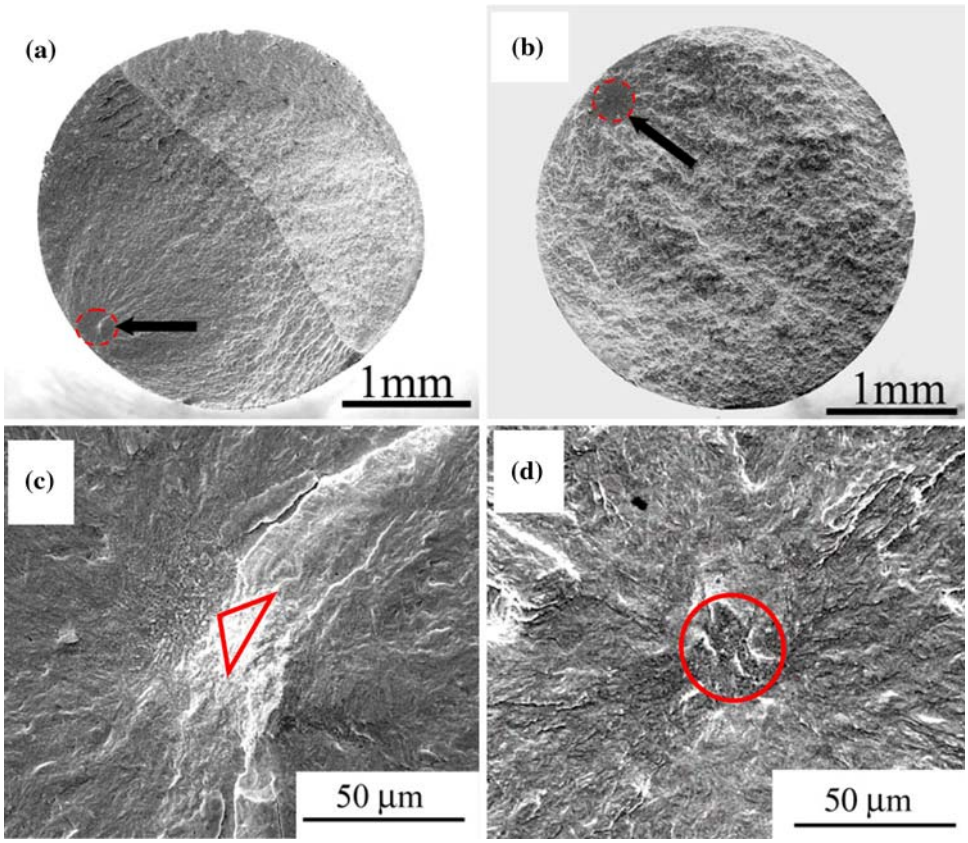

Fig. 6 Observation of scanning electronic microscope of F specimens. **a** No oxidized specimen S3 (σ_a = 650 MPa, $N_f = 1.93 \times 10^7$) and **b** oxidized specimen S4 (σ_a = 650 MPa, $N_f = 1.95 \times 10^6$). **c** and **d** are the enlargement of crack initiation sites of (**a**) and (**b**), respectively

From Ranc et al.'s study [17], as shown in Eq. 2, the dissipated power, noted p, due to formation of per unit of crack length is assumed proportional to the area of the reverse plastic zone.

$$p = \eta f \frac{a^2 \Delta\sigma^4}{36\pi^4 \sigma_y^4} \tag{2}$$

Here the frequency f is a constant of 20 kHz, and a is crack length. The energy is determined by material properties and loading condition, such as yield stress σ_y, applied stress amplitude $\Delta\sigma$, coefficient η depending only on the material. R and F specimens have similar yield stresses. However, the thermal effects are quite different. Half of failed F specimens have oxidized surfaces and none of R specimens is oxidized. The different thermal effects may be explained as follows. The applied stress amplitudes for F specimens are higher than those for R specimens (see Fig. 2). In addition, the yield stress of R specimens (1318 MPa) is slightly higher than that of F specimens (1300 MPa). As shown in Eq. 2 [17], the thermal effect is highly sensitive, with an index of 4, to the quotient of the applied stress amplitude and the yield stress. Therefore, it is not surprise that none of R specimens are oxidized. For the same reason, the stress amplitudes of oxidized specimens are mostly higher than those of no oxidized specimens. The distinct morphologies between inside and outside of fish-eye can be explained as follow. During fish-eye formation, the heat generated is less since the crack size is small. So the temperature rises gradually. Because of low temperature, the specimens would not be oxidized. However, after fish-eye formation, the crack size is larger; the heat generated is much more and the temperature increases abruptly. Then the heat generated by crack propagation is balanced by conduction and convection. Thus, the temperature remains in higher level for a few minutes which causes the specimens surfaces oxidized and roughen the fracture surfaces.

The major experimental results could be well explained by Eq. 2 proposed by Ranc et al. [17]. However, as shown in Fig. 2b, different thermal effects are also observed for a few F specimens under the same applied stress amplitude, for instance S3 and S4 under 650 MPa. It seems that present results for a few specimens do not agree well with Ranc et al.'s prediction [17] according to which the same thermal effects are expected for the same stress amplitude if those eccentricity from the center of the specimens are the same.

In fact, the different thermal effects can be explained by Ranc et al.'s model with a minor modification. From Fig. 6, we notice that the crack of S3 grows more rapidly than that of S4 which means that the da/dN–ΔK curve should have a higher slope, α, higher than 3 [20]. Thus, the curve is approximated by the law [20]:

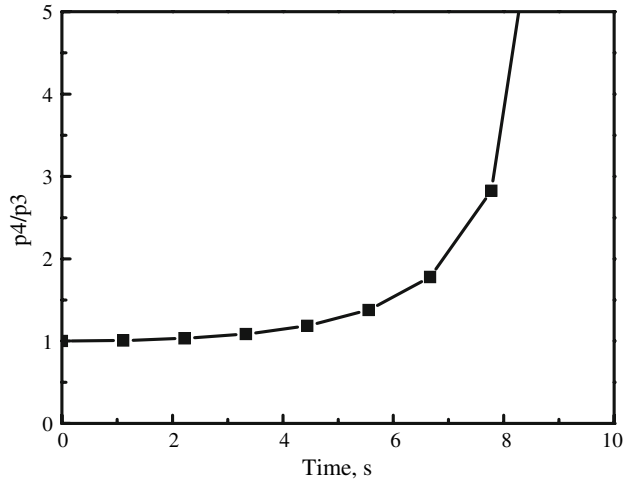

Fig. 7 Evolution of ratio of the dissipated power for different crack growth rate, *p4/p3*. *p4* and *p3* represent the dissipated power for α equals to 4 and 3, respectively

$$\frac{da}{dN} = b\left(\frac{\Delta K_{\text{eff}}}{E\sqrt{b}}\right)^{\alpha} \tag{3}$$

where E is the Young's modulus, b is the norm of the Burgers vector, and ΔK_{eff} is the amplitude of the effective stress intensity factor. On the threshold corner, we have:

$$\frac{da}{dN} = b \quad \text{and} \quad \frac{\Delta K_0}{E\sqrt{b}} = 1$$

The crack growth rata law is thus written:

$$\frac{da}{dN} = b\left(\frac{\Delta K_{\text{eff}}}{E\sqrt{b}}\right)^{\alpha} = b\left(\frac{\Delta K_{\text{eff}}}{\Delta K_0}\right)^{\alpha} = b\left(\frac{a}{a_0}\right)^{\alpha/2}$$

If at time $t = 0$ the crack radius is a_0, then the evolution of crake length, $a(t)$, according to time is

$$a(t) = \frac{a_0}{\left(1 - \frac{t}{t_c}\right)^{\frac{1}{\alpha/2-1}}} \quad \text{with} \quad t_c = \frac{2a_0}{(\alpha-2)bf} \tag{4}$$

By replacing the $a(t)$ in Eq. 2, we obtain

$$p = \frac{p_0}{\left(1 - \frac{t}{t_c}\right)^{\frac{2}{\alpha/2-1}}} \tag{5}$$

with $t_c = \frac{2a_0}{(\alpha-2)bf}$ and $p_0 = \eta f \frac{a_0^2 \Delta\sigma^4}{36\pi^4\sigma_y^4}$. Assuming that α equals to 3 and 4 for S3 and S4, respectively, and other parameters are exactly the same, t_c is 10 *s* for S4 and 20 *s* for S3. As shown in Fig. 7, the dissipated power for S4, *P4*, increases much faster than *P3*, this is, S4 could accumulate a lot of heat in short period of time.

Conclusion

An obvious thermal effect was observed for a bainite/martensite duplex-phase high strength steel under ultrasonic fatigue testing at higher stress amplitudes. After fish-eye formation, the temperature increases and remains in higher level for a few minutes which causes the specimens surfaces oxidized and roughen the fracture surfaces.

Acknowledgements This work was financially supported by National Key Basic Research and Development Program of China (No. G2004CB619100). The authors wish to thank Prof. G. Y. Li for his helpful advices.

References

1. Stanzl-Tschegg S, Mayer H, Tschegg E (1993) Ultrasonics 31:275
2. Bathias C, Paris PC (2005) Gigacycle fatigue in mechanical practice. Marcel Dekker, New York
3. Mayer H (1999) Int Mater Rev 44:1
4. Yang ZG, Li SX, Zhang JM, Li GY, Li ZB, Hui WJ, Weng YQ (2004) Acta Mater 52:5235
5. Yang ZG, Li SX, Liu YB, Li YD, Li GY, Hui WJ, Weng YQ (2008) Int J Fatigue 30:1016
6. Li YD, Yang ZG, Liu YB, Li SX, Li GY, Hui WJ, Weng YQ (2008) Mater Sci Eng A 489:373
7. Liu YB, Yang ZG, Li YD, Chen SM, Li SX, Hui WJ, Weng YQ (2008) Mater Sci Eng A 497:408
8. Liu YB, Yang ZG, Li YD, Chen SM, Li SX, Hui WJ, Weng YQ (2009) Mater Sci Eng A 517:180
9. Bathias C (1999) Fatigue Fract Eng M 22:559
10. Mughrabi H (1999) Fatigue Fract Eng M 22:633
11. Furuya Y, Matsuoka S, Abe T, Yamaguchi K (2002) Scr Mater 46:157
12. Wang QY, Berard JY, Dubarre A, Baudry G, Rathery S, Bathias C (1999) Fatigue Fract Eng M 22:667
13. Marines I, Dominguez G, Baudry G, Vittori J-F, Rathery S, Doucet J-P, Bathias C (2003) Int J Fatigue 25:1037
14. Wang QY, Bathias C (2004) J Mater Sci 39:687. doi: 10.1023/B:JMSC.0000011532.41231.c8
15. Chapetti MD, Tagawa T, Miyata T (2003) Mater Sci Eng A 356:227
16. Meyendorf NG, Rosner H, Kramb V, Sathish S (2002) Ultrasonics 40:427
17. Ranc N, Wagner D, Paris PC (2008) Acta Mater 56:4012
18. Zettl B, Mayer H, Ede C, Stanzl-Tschegg S (2006) Int J Fatigue 28:1583
19. Xue H, Wagner D, Ranc N, Bayraktar E (2006) Fatigue Fract Eng M 29:573
20. Paris PC, Tada H, Donald JK (1999) Int J Fatigue 21:S35